Frequency-Diverse Computational Polarimetic Imaging

Okan Yurduseven, Thomas Fromenteze, Rixi Peng, David Smith

To cite this version:

Okan Yurduseven, Thomas Fromenteze, Rixi Peng, David Smith. Frequency-Diverse Computational Polarimetic Imaging. 13th European Conference on Antennas and Propagation (EuCAP 2019), Mar 2019, Krakow, Poland. hal-02380219

HAL Id: hal-02380219

https://hal.science/hal-02380219v1

Submitted on 26 Nov 2019

Frequency-Diverse Computational Polarimetic Imaging

Okan Yurduseven[1,2], Thomas Fromenteze[3], Rixi Peng[4] and David R. Smith[4]
[1]School of Electronics, Electrical Engineering and Computer Science, Queen's University Belfast, BT3 9DT, United Kingdom, okanyurduseven@ieee.org
[2]Jet Propulsion Laboratory, California Institute of Technology, Pasadena, CA 91109
[3]XLIM UMR 7252, Université de Limoges/CNRS, 87060 Limoges, France
[4]Department of Electrical and Computer Engineering, Duke University, Durham, NC 27708

***Abstract*—In this paper, a frequency-diverse computational polarimetric imaging system is demonstrated at K-band (17.5-26.5 GHz) frequencies. The frequency-diverse operation enables all-electronic data-acquisition by means of a simple frequency-sweep and requires no mechanically moving apparatus or phase shifting circuits for imaging. Leveraging a tensor model for the scattering behavior, as opposed to a scalar model, enables the extraction of further information from the imaged objects. This is shown by means of frequency-diverse polarimetric imaging of complex objects, such as the letters of the word "DUKE", and comparing the reconstructed polarimetric images to the reflectivity-only reconstructions of the same objects.**

***Index Terms*—Imaging, antenna, metasurface, polarimetry, computational.**

I. INTRODUCTION

Computational imaging has gained traction because of its potential to address the challenges of conventional imaging modalities [1-13]. Frequency-diversity is a computational imaging technique that leverages spatially varying radiation patterns to encode the scene information by means of a simple frequency sweep [14-35]. These frequency-dependent radiation patterns are used to illuminate the scene and collect the scattered signal from the scene. As a result, the scene information is encoded onto a set of measurement modes from which an estimate of the scene can be reconstructed using computational imaging techniques. This retrieval process is all-electronic and does not require any mechanical scanning apparatus or phase shifting circuits.

Conventionally, computationally retrieved scene information provides scalar information of the scene, mostly the reflectivity distribution [18]. At microwave and millimeter-wave frequencies, information content of the reconstructed images can be greatly enhanced by leveraging the vectoral relationship between the incident field and the scattered field. This additional set of information, namely polarization, can be used to reveal further information on the geometrical features of the imaged objects. In this paper, we study the retrieval of polarimetric information from computational frequency-diverse imaging. It is shown that by taking into account the tensorial behavior of the scattering from the imaged objects, polarimetric images can be obtained from frequency-diverse measurements.

II. COMPUTATIONAL FREQUENCY-DIVERSE POLARIMETRIC IMAGING

Retrieving the scene information from a set of known measurements is an inverse problem. In frequency-diverse imaging, the measurements are correlated to the scene by means of the following forward model:

$$g(w) = \int_{\mathbf{r}} E_{Tx}(\mathbf{r}, w) E_{Rx}(\mathbf{r}, w) f(\mathbf{r}) d^3\mathbf{r} \tag{1}$$

In (1), g is the measurement vector (as a function of frequency, w), E_{Tx} is the radiated field from the transmit frequency-diverse antennas propagated to the scene, E_{Rx} is the radiated field from the receive frequency-diverse antennas propagated to the scene, f is the reflectivity distribution of the scene, and $\mathbf{r}$ denotes the scene coordinates. For a frequency-diverse imaging system producing M measurement modes and a scene discretized into N voxels, the integral equation of (1) is discretized as follows:

$$\mathbf{g}_{Mx1} = \mathbf{H}_{MxN}\mathbf{f}_{Nx1} + \mathbf{n}_{Mx1} \tag{2}$$

In (2), $\mathbf{n}$ is the system measurement noise. The bold font in (2) is used to denote the vector-matrix notation. Using the first Born approximation, the sensing matrix (or the transfer function of the system) $\mathbf{H}$ can be expressed as proportional to the element-wise matrix multiplication of the transmit and receive frequency-diverse antennas, both of which are propagated to the scene to be imaged, $\mathbf{H} \propto \mathbf{E}_{Tx}\mathbf{E}_{Rx}$ [17]. To retrieve an estimate of the scene information from (2), several computational imaging techniques can be used, from single-shot matched-filter to iterative least-squares algorithms. Using the least-squares algorithm, the scene estimate, $\mathbf{f}_{\text{est}}$, can be obtained as follows [19]:

$$\mathbf{f}_{est} = \arg\min_{\mathbf{f}} \left\| \mathbf{g} - \mathbf{H}\mathbf{f} \right\|_2^2 \tag{3}$$

The retrieved scene information $\mathbf{f}_{\text{est}}$ in (3) is a map of scalar susceptibility distribution of the scene and has a single column vector format (*N*x1 dimension).

In polarimetric imaging, the scalar relationship between the antenna radiated fields and the scene susceptibility is replaced by a vector model, correlating the different polarizations of the transmit and receive fields and a susceptibility *tensor*. For a radar system operating in the far-field, four possible polarization configurations of the transmit and receive fields can be considered; VV, HH, HV and VH, where H denotes the horizontal component and V denotes the vertical component [36, 37]. Operating in the near-field, the interaction between all the three components of the electric-field vectors can be leveraged, resulting in a 3 x 3 susceptibility tensor, $\overline{\overline{\chi}}$, given in (4) [33].

$$\overline{\overline{\chi}} = \begin{bmatrix} \chi_{xx} & \chi_{xy} & \chi_{xz} \\ \chi_{yx} & \chi_{yy} & \chi_{yz} \\ \chi_{zx} & \chi_{zy} & \chi_{zz} \end{bmatrix} \tag{4}$$

Expressing the forward model given in (1) by taking the polarimetry information into account, we obtain the following:

$$g(w) = \int_{\mathbf{r}} E_{Tx}^{i}(\mathbf{r},w)\overline{\overline{\chi}}_{i,j}(\mathbf{r})E_{Rx}^{j}(\mathbf{r},w)d^{3}\mathbf{r} \tag{5}$$

From (5), it is possible to reconstruct the scene information on nine different polarization bases $\overline{\overline{\chi}}_{i,j}$ where $i=x, y, z$ and $j=x, y, z$.

III. IMAGING RESULTS AND DISCUSSION

The frequency-diverse imaging system is shown in Fig. 1.

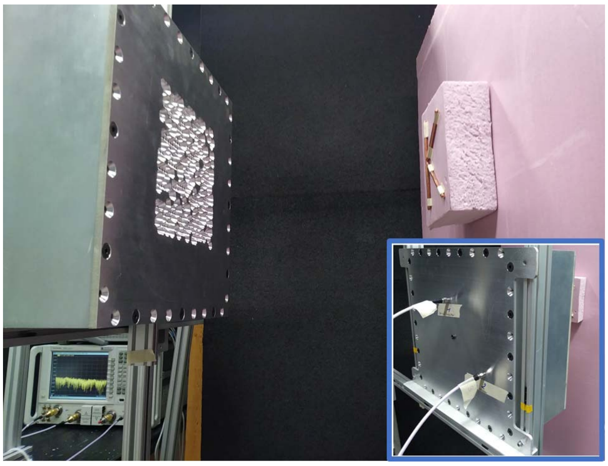

Fig. 1. Frequency-diverse imaging system used for computational polarimetric imaging (feeding ports are shown as inset).

The frequency-diverse imager consists of an air-filled, cavity-backed metasurface antenna interrogating the scene to be imaged at K-band frequencies (17.5-26.5 GHz). The antenna is fed by two ports, port 1 (transmit) and port 2 (receive). Both ports are terminated using an ultra-wideband (UWB) monopole antennas inside the cavity. The dimensions of the cavity-backed metasurface antenna are 15.2 cm x 28.5 cm x 28.5 cm, corresponding to an electrically large loaded cavity supporting multiple mode combinations at K-band frequencies. Feeding the cavity through the first port excites multiple cavity modes which are mixed upon reflections from the cavity walls. The superposed mode patterns inside the cavity are highly diverse. In addition, the cavity antenna has a sphere inclusion embedded inside the cavity in between port 1 and port 2, reducing the direct coupling between the ports and helps mode-mixing [20, 33]. The metasurface consists of an array of subwavelength, circular irises, radiating in dual-polarization. The frequency-dependent cavity modes launched into the cavity by port 1 are sampled by these irises, radiating into free-space and interrogating the imaged object as depicted in Fig. 2.

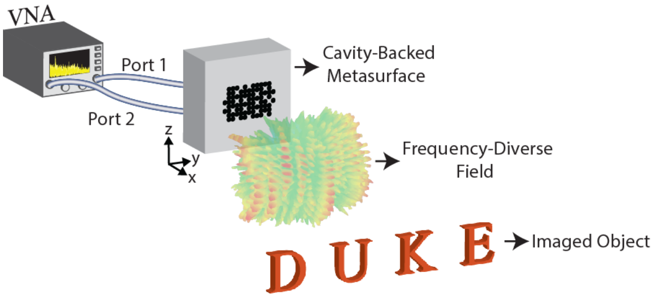

Fig. 2. Frequency-diverse imaging of the letters “D”,”U”, “K”, “E”. The frequency-diverse field interrogating the imaged object is shown at the center frequency, 22 GHz, within the K-band.

The scattered field from the object is received through the second port. Because the cavity-backed metasurface antenna shares the same aperture to transmit and receive, it has a monostatic system layout. Within the scene, the individual letters of the word “DUKE” are present as the imaged object. As shown in Fig. 3(a), the “DUKE” letters were made from an array of copper wires with a diameter of around 5 mm. The object is placed at d=30 cm from the antenna, ensuring sufficient spatial resolution to distinguish the geometrical features of the letters. At d=30 cm distance, the cross-range resolution is δ_{cr}=0.5 cm while the range resolution of the imager is determined by the imaging bandwidth, calculated to be δ_{r}=1.5 cm.

For a frequency-diverse antenna, the orthogonality of the measurement modes interrogating the scene is governed by the quality factor (Q) of the antenna. As a result, having a large Q-factor is important to be able to minimize the redundancy of the information collected from the scene as the frequency is swept. Due to the air-filled structure (no dielectric loss is present) and the polished metal walls (reducing the conduction loss), the Q-factor of the cavity-backed metasurface antenna is high, Q=12000. The Q-factor of the antenna is measured by the decay rate of the time domain impulse response of the antenna [15]. As a result, the upper-bound limit for the number of measurement modes is calculated to be 4901 [14]. In this work, the K-band is sampled at 4001 discrete frequency points, selected in accordance with the theoretical upper bound limit. The scene is discretized into N=8000 cubic voxels, and for image reconstruction, the least squares-algorithm is used [19].

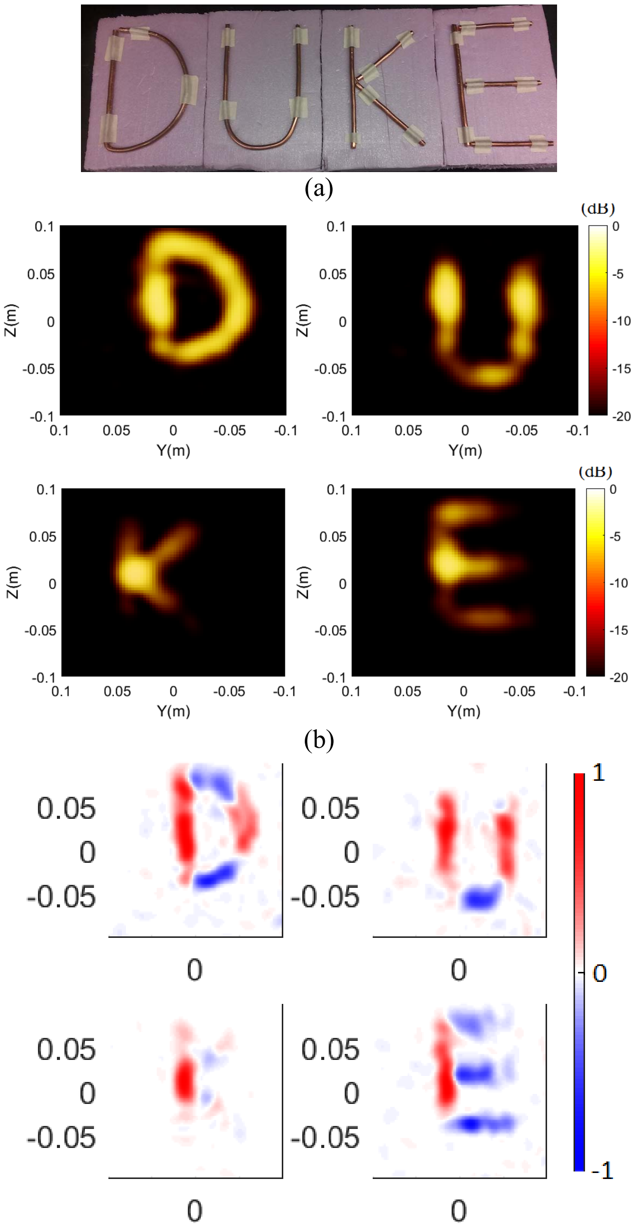

(a)

(b)

(c)

Fig. 3. Imaging of the letters "DUKE" (a) actual imaged object (b) scalar reconstructed image (intensity) (c) polarimetric image.

The reconstructed images in Fig. 3(b) present the scalar susceptibility distribution of the "DUKE" letters. In addition to the intensity information, the reconstructed images in Fig. 3(c) provide polarimetric information. It is well-known in electromagnetic (EM) theory that electric-field (E-field) incident upon a wire along its longitudinal axis induces a current distribution along the longitudinal axis, re-radiating in the same direction. Based on this principle, a vertical wire with an impinging E-field in the vertical direction, scatters a vertically-polarized E-field while a horizontal wire with an impinging horizontally polarized E-field scatters an E-field in the horizontal direction. In Fig. 3(c), this phenomenon is evident. The vertical wires are excited by a vertically-polarized incident E-field and appear in vertical polarization (coded in red). The horizontal wires are excited by a horizontally polarized incident E-field and appear in horizontal polarization (coded in blue).

IV. CONCLUSION

We have demonstrated the application of polarimetry to computational frequency-diverse imaging. Different from the scalar susceptibility model, the polarimetric computational imaging leverages a tensor model, interacting the different polarization states of the antenna radiated fields incident upon and reflected from the imaged object. Leveraging polarimetry, further information about the geometrical features of the imaged objects can be extracted. The demonstrated polarimetric computational imaging system exhibits all-electronic operation and requires no phase shifting circuits, significantly simplifying the physical hardware layer of the system. Although demonstrated for microwave frequencies, it can reality be scaled to higher frequencies, where finer resolution limits and smaller antennas are required.

REFERENCES

[1] J. Hunt, T. Driscoll, A. Mrozack, G. Lipworth, M. Reynolds, D. Brady, and D. R. Smith, "Metamaterial apertures for computational imaging," Science, vol. 339, no. 6117, pp. 310-313, 2013.

[2] D. J. Brady, Optical imaging and spectroscopy, John Wiley & Sons, 2009.

[3] D. Shrekenhamer, C. M. Watts, and W. J. Padilla, "Terahertz single pixel imaging with an optically controlled dynamic spatial light modulator," Opt. Express, vol 21, no. 10, pp. 12507-12518, 2013.

[4] T. Fromenteze, C. Decroze, S. Abid, and O. Yurduseven, "Sparsity-Driven Reconstruction Technique for Microwave/Millimeter-Wave Computational Imaging," Sensors, vol. 18, no. 5, p.1536, 2018.

[5] S. Caorsi, A. Massa and M. Pastorino, "A computational technique based on a real-coded genetic algorithm for microwave imaging purposes," *IEEE Transactions on Geoscience and Remote Sensing*, vol. 38, no. 4, pp. 1697-1708, July 2000.

[6] M. Donelli, and A. Massa, "Computational approach based on a particle swarm optimizer for microwave imaging of two-dimensional dielectric scatterers," *IEEE Transactions on Microwave Theory and Techniques*, vol. 53, no. 5, pp.1761-1776, 2005.

[7] T. Sleasman, M. Boyarsky, M. F. Imani, J. N. Gollub, and D. R. Smith, "Design considerations for a dynamic metamaterial aperture for computational imaging at microwave frequencies," *JOSA B*, vol. 33, no. 6, pp.1098-1111, 2016.

[8] A. Molaei *et al.*, "3D Printed E-Band Compressive Horn Antenna for High-sensing-capacity Imaging Applications," *IEEE Antennas and Wireless Propagation Letters,* 2018.

[9] R. Obermeier and J. A. Martinez-Lorenzo, “Sensing matrix design via mutual coherence minimization for electromagnetic compressive imaging applications,” *IEEE Transactions on Computational Imaging*, vol. 3, no. 2, pp. 217-229, 2017.

[10] Y. Álvarez, Y. Rodriguez-Vaqueiro, B. Gonzalez-Valdes, C. M. Rappaport, F. Las-Heras and J. Á. Martínez-Lorenzo, "Three-Dimensional Compressed Sensing-Based Millimeter-Wave Imaging," *IEEE Transactions on Antennas and Propagation*, vol. 63, no. 12, pp. 5868-5873, Dec. 2015.

[11] E. Kpré, C. Decroze, M. Mouhamadou, and T. Fromenteze, “Computational Imaging for Compressive Synthetic Aperture Interferometric Radiometer (CSAIR),” *IEEE Transactions on Antennas and Propagation*, 2018

[12] E. L. Kpré, C. Decroze, and T. Fromenteze, “MIMO radar pseudo-orthogonal waveform generation by a passive 1× M mode-mixing microwave cavity,” *International Journal of Microwave and Wireless Technologies*, vol. 9, no. 7, pp. 1357-1363, 2017.

[13] T. Sleasman, M. Boyarsky, M. F. Imani, T. Fromenteze, J. N. Gollub, and D. R. Smith, “Single-frequency microwave imaging with dynamic metasurface apertures,” *JOSA B*, vol. 34, no. 8, pp.1713-1726, 2017.

[14] D. L. Marks, J. Gollub, and D. R. Smith, “Spatially resolving antenna arrays using frequency diversity,” *J. Opt. Soc. Am. A*, vol. 33, no. 5, pp. 899-912, 2016.

[15] O. Yurduseven, J. Gollub, D. Marks, *et al.*, “Frequency-diverse microwave imaging using planar Mills-Cross cavity apertures,” *Opt. Express*, vol. 24, no. 8, pp. 8907-892, 2016.

[16] G. Lipworth, A. Mrozack, J. Hunt, et al., “Metamaterial apertures for coherent computational imaging on the physical layer,” *J. Opt. Soc. Am. A*, vol. 30, no. 8, pp. 1603-1612, 2013.

[17] G. Lipworth, A. Rose, O. Yurduseven, *et al.*, “Comprehensive simulation platform for a metamaterial imaging system,” *Appl. Opt.*, vol. 54, no. 31, pp. 9343-9353, 2015.

[18] J. Hunt, J. Gollub, T. Driscoll, *et al.*, “Metamaterial microwave holographic imaging system,” *J. Opt. Soc. Am. A*, vol. 31, no. 10, pp. 2109–2119, 2014.

[19] O. Yurduseven, M. F. Imani, H. Odabasi, *et al.*, “Resolution of the frequency diverse metamaterial aperture imager,” *Prog. Electromagnetics Res.*, vol. 150, pp. 97-107, 2015.

[20] T. Fromenteze, O. Yurduseven, M. F. Imani, *et al.*, “Computational imaging using a mode-mixing cavity at microwave frequencies,” *Appl. Phys. Lett.*, vol. 106, pp. 194104, 2015.

[21] O. Yurduseven, V. R. Gowda, J. Gollub, *et al.,* “Printed aperiodic cavity for computational microwave imaging,” *IEEE Microw. Wirel. Compon. Lett.*, vol. 26, no. 5, pp. 367-369, 2016.

[22] O. Yurduseven, V. R. Gowda, J. N. Gollub, *et al.*, “Multistatic microwave imaging with arrays of planar cavities,” *IET Microwaves, Antennas & Propagation*, vol. 10, no. 11, pp. 1174-1181, 2016.

[23] O. Yurduseven, J. N. Gollub, K. P. Trofatter, *et al.,* “Software calibration of a frequency-diverse, multistatic, computational imaging system,” *IEEE Access*, vol. 4, pp. 2488-2497, 2016.

[24] D. L. Marks, O. Yurduseven, and D. R. Smith, “Fourier Accelerated Multistatic Imaging: A Fast Reconstruction Algorithm for multiple-input-multiple-output (MIMO) radar imaging,” *IEEE Access*, vol. 5, pp. 1796-1809, 2017.

[25] D. L. Marks, O. Yurduseven, and D. R. Smith, “Hollow Cavity Metasurface Aperture Antennas and Their Application to Frequency Diversity Imaging,” *Journal of the Optical Society of America A*, vol. 34, no. 4, pp. 472-480, 2017.

[26] O. Yurduseven, J. N. Gollub, A. Rose, *et al.*, “Design and Simulation of a Frequency-Diverse Aperture for Imaging of Human-Scale Targets,” *IEEE Access*, vol. 4, pp. 5436-5451, 2016.

[27] J. N. Gollub, O. Yurduseven, K. P. Trofatter, *et al.,* “Large Metasurface Aperture for Millimeter Wave Computational Imaging at the Human-Scale,” *Scientific Reports*, vol. 7, pp. 42650, 2017

[28] O. Yurduseven, D. L. Marks, T. Fromenteze, J. N. Gollub, and D. R. Smith, “Millimeter-wave spotlight imager using dynamic holographic metasurface antennas,” *Optics Express*, vol. 25, no. 15, pp.18230-18249, 2017.

[29] O. Yurduseven, D. L. Marks, J. N. Gollub, and D. R. Smith, “A reconfigurable millimeter-wave spotlight metasurface aperture integrated with a frequency-diverse microwave imager for security screening,” Passive and Active Millimeter-Wave Imaging XXI, International Society for Optics and Photonics, vol. 10634, pp. 1063406, 2018.

[30] O. Yurduseven, D. L. Marks, T. Fromenteze, and D. R. Smith, “Dynamically reconfigurable holographic metasurface aperture for a Mills-Cross monochromatic microwave camera,” *Optics Express*, vol. 26, no. 5, pp. 5281-5291, 2018.

[31] O. Yurduseven, T. Fromenteze, and D. R. Smith, “Relaxation of Alignment Errors and Phase Calibration in Computational Frequency-Diverse Imaging using Phase Retrieval,” *IEEE Access*, vol. 6, pp. 14884-14894, 2018.

[32] D. L. Marks, O. Yurduseven, and D. R. Smith, “Sparse blind deconvolution for imaging through layered media,” Optica, vol. 4, no. 12, pp. 1514-1521, 2017.

[33] T. Fromenteze, O. Yurduseven, M. Boyarsky, J. Gollub, D. L. Marks, and D. R. Smith, “Computational polarimetric microwave imaging,” Optics Express, vol. 25, no. 22, pp. 27488-27505, 2017.

[34] O. Yurduseven, P. Flowers, S. Ye, D. L. Marks, J. N. Gollub, T. Fromenteze, B. J. Wiley, and D. R. Smith, “Computational microwave imaging using 3D printed conductive polymer frequency-diverse metasurface antennas,” *IET Microwaves, Antennas & Propagation*, vol. 11, no. 14, pp.1962-1969, 2017.

[35] D. L. Marks, O. Yurduseven, and D. R. Smith, “Near-field multistatic radar reconstruction with stretched-phase Fourier accelerated multistatic imaging,” *IET Radar, Sonar & Navigation*, vol. 11, no. 11, pp.1718-1729, 2017.

[36] S. C. M. Brown and J. C. Bennett, "High-resolution microwave polarimetric imaging of small trees," in *IEEE Transactions on Geoscience and Remote Sensing*, vol. 37, no. 1, pp. 48-53, Jan. 1999.

[37] J. S. Lee, and E. Pottier, Polarimetric Radar Imaging, Boca Raton: CRC Press, 2009.